Load Sharing between Austenite and Ferrite in a Duplex Stainless Steel during Cyclic Loading

JOHAN JOHANSSON and MAGNUS ODÉN

The load sharing between phases and the evolution of micro- and macrostresses during cyclic loading has been investigated in a 1.5-mm cold-rolled sheet of the duplex stainless steel SAF 2304. X-ray diffraction (XRD) stress analysis and transmission electron microscopy (TEM) show that even if the hardness and yield strength are higher in the austenitic phase, more plastic deformation will occur in this phase due to the residual microstresses present in the material. The origin of the microstresses is the difference in coefficients of thermal expansion between the two phases, which leads to tensile microstresses in the austenite and compressive microstresses in the ferrite. The microstresses were also found to increase from 50 to 140 MPa in the austenite during the first 100 cycles when cycled in tension fatigue with a maximum load of 500 MPa. The cyclic loading response of the material was, thus, mainly controlled by the plastic properties of the austenitic phase. It was also found that initial compressive macrostresses on the surface increased from −40 to 50 MPa during the first 10^3 cycles. After the initial increase of microstresses and macrostresses, no fading of residual stresses was found to occur for the following cycles. A good correlation was found between the internal stress state and the microstructure evolution. The change in texture during cyclic fatigue showed a sharpening of the deformation texture in the ferritic phase, while no significant changes were found in the austenitic phase.

I. INTRODUCTION

DUPLEX stainless steels, consisting of approximately equal amounts of austenite and ferrite, are established today in a wide product range from chemical tankers, pressure vessels, and pipes to heat exchangers, paper machines, and offshore applications. The high strength of the duplex grades enables both weight and cost savings when they are used as corrosion resistant materials in a construction. The use of duplex stainless steels in load carrying applications has increased the demand for thorough knowledge of the fatigue mechanisms in these materials. Magnin *et al.*[1,2] studied the low-cycle fatigue behavior of the duplex alloy 22Cr-7Ni-2.5Mo-1.7Mn-0.07N. They found that crack initiation was related to the cyclic deformation mechanisms of ferrite at high plastic strain amplitudes ($\varepsilon_{pl} > 10^{-3}$) and to those of austenite at relatively low ε_{pl}. These results are supported by later studies on duplex stainless steels with higher nitrogen content.[3,4]

Degallaix *et al.*,[5] on the other hand, investigated the duplex alloy 22.1Cr-5.4Ni-3.1Mo-1.7Mn-0.11N, in wt pct, and 22.2Cr-5.5Ni-3.1Mo-0.9Mn-0.18N and found that crack initiations were observed exclusively in the ferrite at low-strain amplitudes and indifferently in both phases at higher strain amplitudes. Similar results are found by Polak *et al.*[6] who studied polished specimens of duplex stainless steel type 2205 with 0.11 pct nitrogen. They found that crack initiation starts at persistent slip bands in the ferrite. The persistent slip bands were generally more numerous in the ferritic grains, and only a few cracks were initiated at slip markings in the austenitic grains.

JOHAN JOHANSSON, Graduate Student, and MAGNUS ODÉN, Research Associate, are with the Division of Engineering Materials, Department of Mechanical Engineering, Linköping University, S-581 83 Linköping, Sweden.

Manuscript submitted August 23, 1999.

These inconclusive results might be explained by the internal stress state in the material. Residual microstresses are always present in duplex stainless steels due to the difference in coefficient of thermal expansion between the two phases. A large variation in residual thermal stresses, both measured and calculated, has been reported in the literature,[7–10] and it is clear that texture effects and plastic relaxation will influence these stresses.[9] Johansson *et al.*[9] has shown that these residual microstresses can change during deformation due to different elastic and plastic properties of the two phases. It is, therefore, likely that microstresses influence the plastic strain and, thus, also the cyclic slip localization causing fatigue crack initiation.

Residual stresses in a material can be measured by X-ray diffraction (XRD) using well-established procedures.[11] This technique allows for determination of the triaxial stress tensor in each phase separately and has been successfully used for studying load sharing between phases and effects of microstresses on the fatigue behavior in a 1080 steel.[12–15] Winholtz and Cohen[15] found that the fraction of load taken by the carbides greatly increases as the steel deforms during low-cycle fatigue. They also found that the morphology has an impact on the development of microstresses. The stress response of the individual phases in a 1080 steel with pearlitic and spheroidal microstructure, respectively, was investigated. It was found that the microstresses were higher in the pearlitic condition than in the spheroidized condition. They concluded that these differences arise from the morphology; the pearlite lamellae more effectively transfer the load to the cementite phase. The higher microstresses give the pearlitic condition a higher work-hardening rate than the spheroidized condition.

Winholts and Cohen[14] have also investigated changes in the macrostress and microstress in steel during high-cycle fatigue. They found that in heat-treated specimens of pearlite, spheroidite, and tempered martensite with no initial residual stresses, no development of residual stresses occurs for fully reversed uniaxial fatigue loading. Both macro-stresses initially present in the material due to shot peening and microstresses fade with fatigue.

The effect of residual macrostresses and microstresses on fatigue crack initiation and propagation in 1080 steel has also been studied by Almer *et al.*[12,13] Residual stresses were introduced into double-edge notched specimens by prestraining and press-fit operations. Microstresses were observed to fade rapidly during fatigue, while macrostresses relaxed less rapidly and were observed to strongly affect crack initiation behavior. They also found that residual microstresses do not affect stage II fatigue crack propagation. This can be attributed to microstress fading within the crack tip strain field. However, fatigue crack growth rates increased in the presence of tensile residual macrostresses, and these increases appear to occur earlier during growth with a decreasing stress intensity factor range.

In this article, we report the evolution of the internal stress state of a duplex stainless steel during tension fatigue. The observed stress changes, measured with XRD, are correlated to the microstructure evolution, studied by transmission electron microscopy (TEM) and XRD texture analysis.

II. EXPERIMENTAL PROCEDURES

A. *Specimens*

The material is a commercial duplex stainless steel of type SAF 2304 provided by Avesta Sheffield AB (Nyby, Sweden). The chemical composition is given in Table I. The steel has been hot and cold rolled to a thickness of 1.5 mm. After rolling, the material was quenched from a temperature of 1050 °C to avoid precipitation of secondary phases. The micrograph in Figure 1 shows, as a result of hot rolling, a heavily banded microstructure with austenitic islands in a ferritic matrix. The volume fraction, determined from point counting of each phase, is 45 ± 5 pct for the ferritic phase and 55 ± 5 pct for the austenitic phase. The size of the austenitic islands scatters with typical values in the range of 0.5 to 3.0 μm in the normal direction, 5 to 25 μm in the transverse direction, and 15 to 200 μm in the rolling direction. The distance between the austenitic islands is typically 3 μm in the normal, 25 μm in the transverse, and 150 μm in the rolling direction. The grain size of the ferritic phase is about 10 μm in the rolling and transverse directions and 1.5 μm in the normal direction. Due to recrystallization after cold rolling, each austenite island consists of several grains with typical values in the range of 0.5 to 3.0 μm in all directions, and the size of the austenitic grains are generally smaller than the ferritic grains. No secondary phases were observed in the optical micrographs or in the X-ray diffractograms.

Macroscopic mechanical properties for the investigated material are listed in Table II. In a previous study,[9] it was found that the hardness and yield strength are higher for the austenitic phase than the ferritic phase. It was also found that the elastic anisotropy present in the material is mainly caused by crystallographic texture in the ferritic phase.

Table I. Chemical Composition of the Duplex Stainless Steel SAF 2304

Element	Fe	C	Si	Mn	Cr	Ni	Mo	Cu	N
Fraction (wt pct)	bal	0.022	0.37	1.5	22.8	4.9	0.31	0.26	0.098

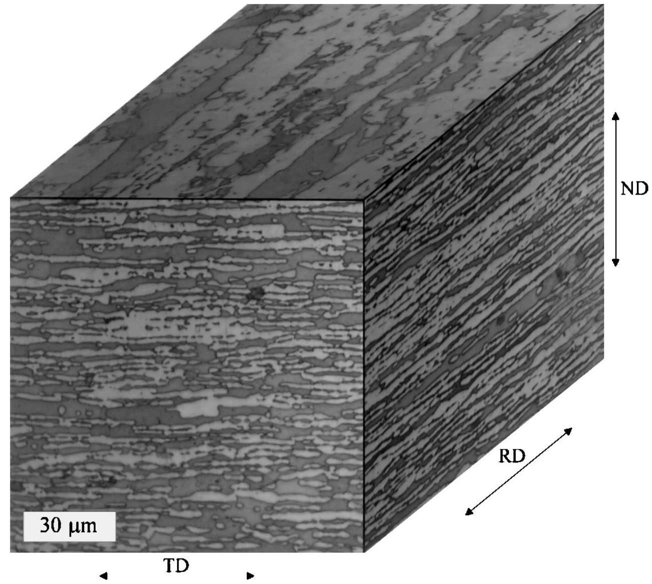

Fig. 1—Microstructure of the duplex stainless steel SAF 2304. Austenite is the bright etching phase and ferrite is the dark phase.

Table II. Macroscopic Material Properties of Duplex Stainless Steel SAF 2304[9]

Properties	RD	45*	TD	Method
Young's modulus (GPa)	196	199	209	resonance testing
Proof strength $R_{p0.2}$ (MPa)	523	530	566	tensile test
Tensile strength R_m (MPa)	730	713	767	tensile test
Strain to failure (pct)	39	43	38	tensile test

*The 45 direction is 45 deg between RD and TD.

Flat specimens with a thickness of 1.5 mm, width of 8.0 mm, and gage length of 70 mm were machined from the sheet with the rolling direction corresponding to the loading axis. After machining, the specimens were ground with 1200-grit SiC paper followed with 6, 3, and 1 μm diamond paste. After mechanical surface treatment, 10 μm was electropolished away from the specimens to avoid grinding stresses at the surface.

B. *Fatigue Testing*

Pulsating ($R = 0.05$) stress-controlled fatigue testing was performed in a servohydraulic Instron/MTS testing machine with a maximum capacity of 40 kN. The elongation of the fatigue specimens has been monitored using an extensometer with a gauge length of 25 mm. The tests were carried out with a frequency of 1.0 Hz with a maximum load of 500 MPa. The test was interrupted after 10, 10^2, 10^3, 10^4, 10^5, and $3.5 \cdot 10^5$ cycles, and the specimens were then moved to a tensile test device constructed to fit on the X-ray diffractometer. The last fatigue cycle was then performed on the diffractometer where phase specific stresses were measured *in situ* during loading. The stresses were recorded at different load steps, corresponding to 0, 400, and 500 MPa during loading and 100 and 0 MPa during unloading.

C. *Stress Measurements by XRD*

X-ray diffraction gives the opportunity to measure the total stress tensor separately in each phase of a two-phase material if the unstressed lattice parameters of the phases are well known. When the total stress tensors are known, one can extract the macrostress and microstress tensors.

Macrostresses are by definition the same in both phases of a two-phase material[16] and can be caused by an external applied load or arise from differential deformation of one region of a material with respect to another. These stresses vary slowly on a scale that is large compared to the material's microstructure. Microstresses, however, vary on the scale of the material's microstructure and must balance between the phases.[16] The microstresses may arise in a number of different ways such as mechanical deformation and heat treatment of a two-phase material with different elastic, plastic, and thermal properties of the individual phases. The average total stress, $\langle {}^{t}\sigma_{ij}^{\alpha} \rangle$, at any point in phase α is the sum of the macro- and microstress components

$$\langle {}^{t}\sigma_{ij}^{\alpha} \rangle = {}^{M}\sigma_{ij} + \langle {}^{\mu}\sigma_{ij}^{\alpha} \rangle \qquad [1]$$

where the superscript α denotes phase α, M is the macrostress, and μ is the microstress. The average total stress in a phase is what a diffraction measurement can reveal. To separate the total stress into macro- and microstresses, one needs to use the equilibrium conditions. For any stress component σ_{ij} in a two-phase material, the following relation holds:

$$(1 - V_f)\,\langle {}^{\mu}\sigma_{ij}^{\alpha} \rangle + V_f\,\langle {}^{\mu}\sigma_{ij}^{\beta} \rangle = 0 \qquad [2]$$

where V_f denotes the volume fraction of phase β, and where the angle braces imply averages over the appropriate volume.[11] By determining the total stress for each phase from measurements and using Eqs. [1] and [2], the macro- and microstresses can be separated.

An Ω diffractometer with Cr K_α radiation was used to measure the interplanar spacing of the {211} planes in the ferritic phase and of the {220} planes in the austenitic phase. In order to make three-dimensional (3-D) stress analysis possible, lattice displacements were determined in 3 ϕ directions (0, 60, and 120 deg) for 11 ψ angles between $\pm$50 deg for the ferrite and between $\pm$42 deg for the austenite. For a definition of the preceeding angles, see Reference 11. The locations of the diffracted peaks were determined by a least-squares fit of a pseudo-Voigt function to the data. The unstressed lattice parameters a_0 for each phase in the investigated material were determined previously to be 3.59694 $\pm$ 0.00020 Å for austenite and 2.87355 $\pm$ 0.00018 Å for ferrite.[9] The stress tensor was determined in each phase by a least-squares procedure,[17] where the Hill average of the single crystal values given by Lebrun and Inal[18] was used as the X-ray elastic constants. The total stress tensors were than separated into macro- and microstress tensors for each phase using Eqs. [1] and [2].

Throughout this study, no texture effects have been included when the stresses were calculated from the measured lattice strains. This is justified by previous studies by Inal and Lebrun.[18,19] They investigated the influence of X-ray elastic constants (XEC) on the residual stresses in a duplex stainless after plastic deformation and found that the determined stresses are insignificantly affected when using anisotropic XEC instead of isotropic XEC values. They offer two possible explanations. (1) The {211} planes for ferrite and {220} planes for austenite have a crystallographic factor[20] equal to 0.25, which is close to the 0.20 value corresponding to isotropic behaviors. (2) The anisotropic elastic effect is low compared to the plastic one. The negligence of texture effects is also justified by the almost linear dependency of lattice spacing on $\sin^2 \psi$.

D. *Microstructure Evolution*

The microstructure evolution and the dislocation substructure characterization of the fatigued specimens were carried out through TEM studies and XRD-texture measurements. The surfaces of the fatigued specimens were also examined by optical and electron microscopy to reveal slip mark formation.

The crystallographic texture of both phases was determined for the material as received and after 10, 10^3, 10^4, and 10^5 cycles by XRD-texture measurements on a Seifert PTS 3000 diffractometer using Co K_α radiation. Four incomplete pole figures were measured for each phase by the Shultz reflection method: {110}, {200}, {211}, and {220} for the ferritic and {111}, {200}, {220}, {311} for the austenitic phase. Correction factors for defocusing were obtained from a texture-free powder sample. The texture was investigated in greater detail using orientation distribution functions (ODFs) calculated by the series expansion method.[21]

For the TEM studies, disks with a diameter of 3 mm and the foil plane parallel to the tensile axis were punched from both the surface and the interior of the fatigued specimens. The disks were reduced to a thickness of 50 to 100 μm by mechanical polishing. Foils were finally produced by electropolishing to perforation using a solution of 1000 mL CH_3COOH, 75 mL $HClO_4$, and 45 mL H_2O in a Struers Tenupol-3 electrolytic polishing equipment. The dislocation structures were then examined in a PHILIPS* EM400T microscope operating at 120 kV.

* PHILIPS is a trademark of Philips Electronic Instruments Corp., Mahwah, NJ.

III. RESULTS

A. *Fatigue Testing*

Fatigue tests were performed under pulsating stress control ($R = 0.05$) with a maximum load of 500 MPa. This load corresponds to a fatigue life of approximately $4.2 \cdot 10^5$ cycles. The hysteresis loops for different load cycles, recorded during the fatigue testing, are shown in Figure 2. The hysteresis loops of all cycles, except the first one, exhibit almost the same width. Because the fatigue tests were performed in stress-controlled fatigue with a nonzero mean stress, a pronounced ratchetting is apparent in Figure 2. The accumulation of plastic strain in each load cycle will of course influence the measured microstresses, and different results must be expected if the fatigue testing was performed with a zero or negative mean stress. The total strain range *vs* number of cycles is plotted in Figure 3 and shows that rapid hardening during the first cycles is followed by slow softening.

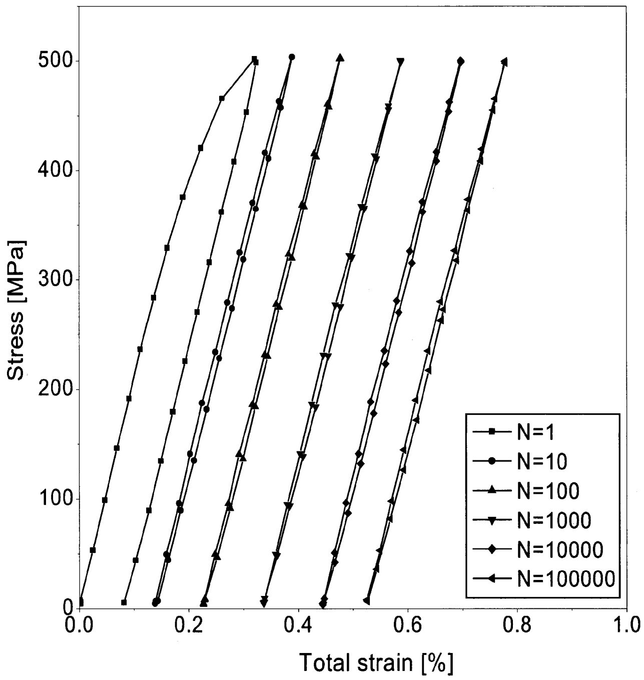

Fig. 2—Hysteresis loops for different fatigue cycles.

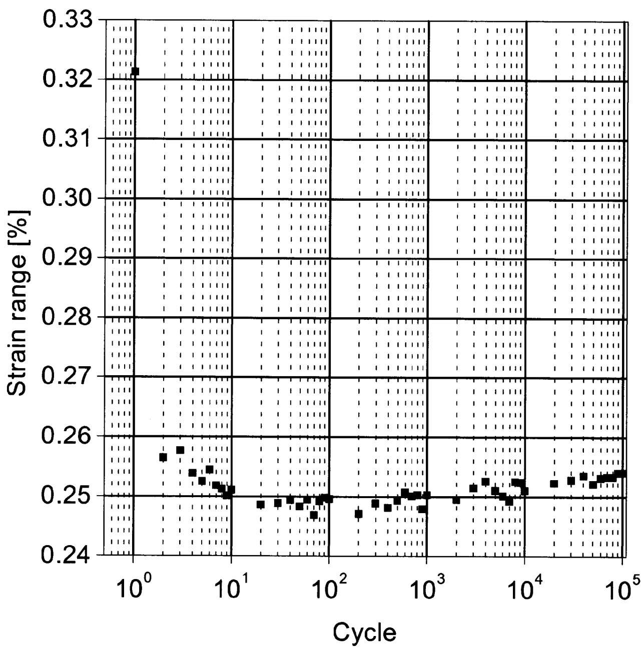

Fig. 3—Total strain range as a function of number of load cycles.

B. *Stresses Measured with XRD*

The total triaxial stress tensors in the ferritic and austenitic phase, ${}^t\sigma^\alpha$ and ${}^t\sigma^\gamma$, were measured with XRD and separated into macrostresses and microstresses for each phase. Stresses for cycle numbers 1, 10, 10^2, 10^3, 10^4, 10^5 and $3.5 \cdot 10^5$ were measured at five different load steps along the load cycle at 0, 400, and 500 MPa during loading and at 100 and 0 MPa during unloading. Due to significantly different coefficients of thermal expansion,[9] phase specific residual microstresses are introduced as a result of quenching from a stress-free temperature. Figure 4 shows the evolution during fatigue of the residual microstresses in the unloaded specimens.

The stresses in the rolling direction, which is also the direction of applied load, increase during the first hundred cycles and then reach a saturation stage (Figure 4(a)). The stresses in the other two directions show similar trends, but the changes are smaller and fall within the error range (Figures 4(b) and (c)). The microstresses at maximum applied load increase slightly in the loading direction but follow no significant trend in the other two directions (Figure 5).

Because X-ray stress analysis completely separates the stress arising in the ferrite from the stress arising in the austenite, the load sharing between the two phases during one load cycle can be established. A load-sharing index L_i, therefore was defined as

$$L_i = V_f^\alpha \cdot \frac{\langle {}^t\sigma_{RD}^\alpha \rangle_i^{\mathrm{MAX}} - \langle {}^t\sigma_{RD}^\alpha \rangle_i^{\mathrm{MIN}}}{\langle {}^M\sigma_{RD} \rangle_i^{\mathrm{MAX}} - \langle {}^M\sigma_{RD} \rangle_i^{\mathrm{MIN}}} \qquad [3]$$

where V_f^α is the volume fraction of the ferritic phase. $\langle {}^t\sigma_{RD}^\alpha \rangle_i^{\mathrm{MAX}}$ and $\langle {}^t\sigma_{RD}^\alpha \rangle_i^{\mathrm{MIN}}$ denote the maximum and minimum average total stress in the ferritic phase for cycle *i*, and $\langle {}^M\sigma_{RD} \rangle_i^{\mathrm{MAX}}$ and $\langle {}^M\sigma_{RD} \rangle_i^{\mathrm{MAX}}$ denote the maximum and minimum macrostress for cycle *i*. This index has the following properties: when L_i is equal to 0, all load is taken by the austenite; when L_i is equal to 1, all load is taken by the ferrite; and when L_i is equal to 0.5, both phases take the same amount of load. Notice that when L_i is equal to V_f^α, both phases transfer the same amount of load per unit area and, thus, both phases have similar elastoplastic behavior. Figure 6 shows the load-sharing index as a function of load cycles. It can be seen that the austenitic phase behaves similarly to the ferritic phase for the first cycle, but for the following cycles, more load per unit area is transferred through the ferrite. A maximum in the load sharing index is found around cycle 400. This maximum is followed by a decrease in the load-sharing index, which indicates a hardening of the austenitic phase, at least on the surface where the stresses are measured. It is important to note that residual microstresses influence the load-sharing index strongly, and this index should, therefore, not be taken directly as a measure of, for instance, yield strength.

A clearer picture of the load-sharing mechanisms is seen if one studies the hysteresis loops separately for the two phases. In Figure 7, the measured average total stresses in both phases are plotted as a function of the applied macroscopic total strain for different cycles. One can see here that the relative width of the hysteresis loops between the two phases changes during fatigue. While the hysteresis loops in the austenite show minor changes after the very first cycles, there is a trend toward decreasing width of the hysteresis loops in the ferritic phase with increasing number of cycles.

The width, defined as the full-width at half-maximum (FWHM), of the diffracting peak is, in this case, a measure of the relative degree of inhomogeneous deformation and dislocation density present in different samples. In Figure 8, the FWHM is plotted as a function of load cycles for both phases in the unloaded condition and when the specimen is subjected to maximum load. During cyclic loading, an

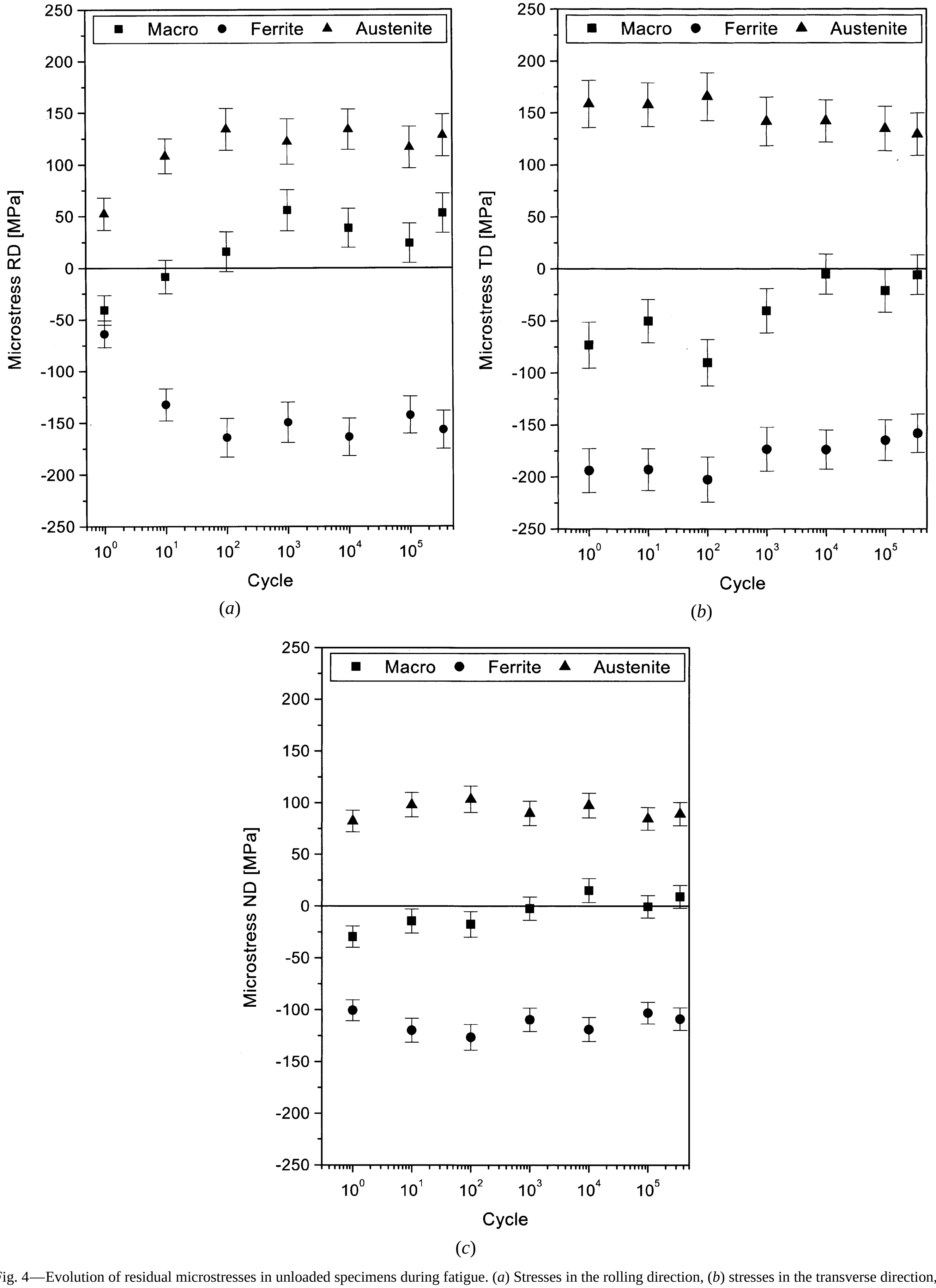

Fig. 4—Evolution of residual microstresses in unloaded specimens during fatigue. (*a*) Stresses in the rolling direction, (*b*) stresses in the transverse direction, and (*c*) stresses in the normal direction.

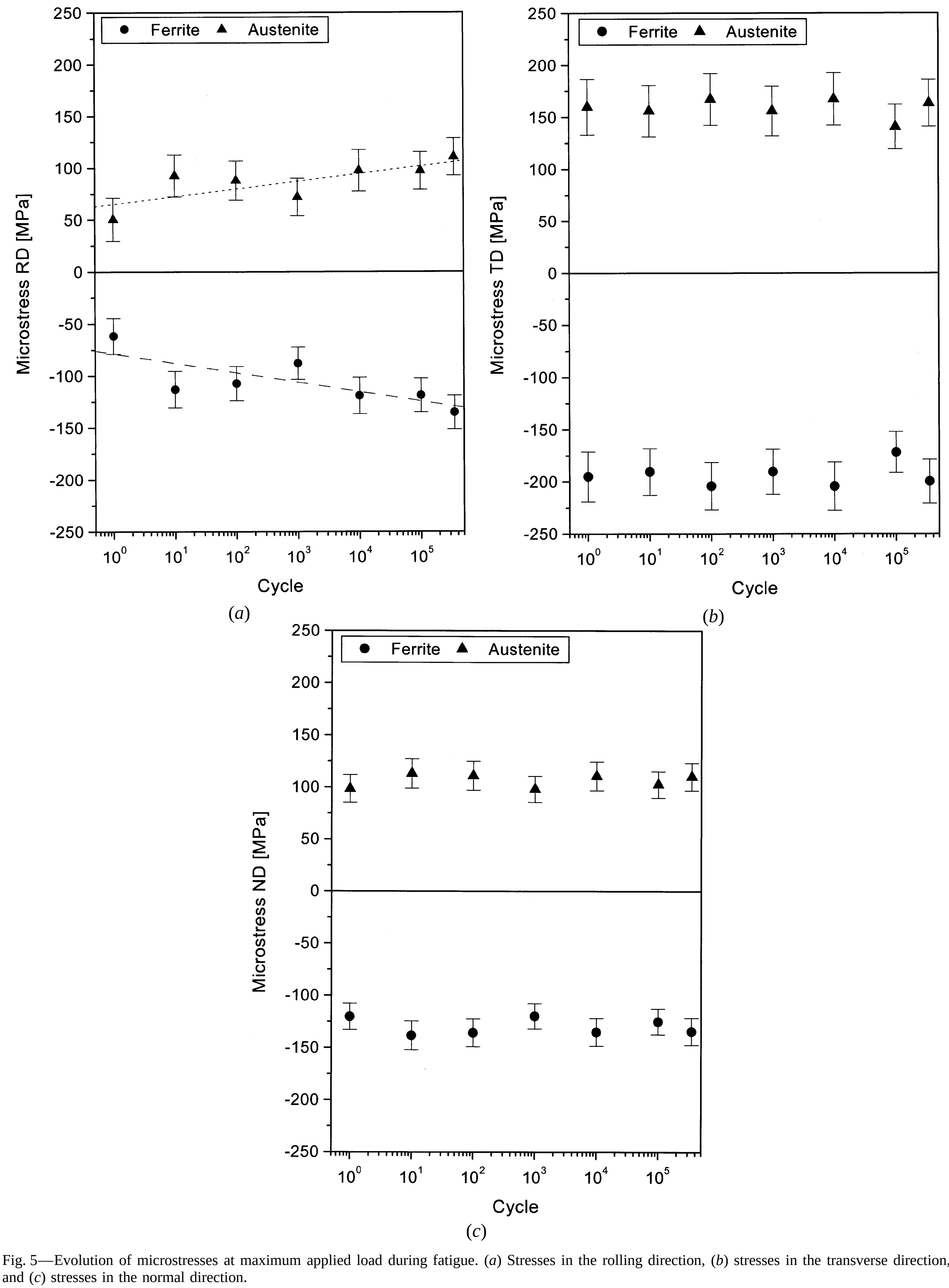

Fig. 5—Evolution of microstresses at maximum applied load during fatigue. (*a*) Stresses in the rolling direction, (*b*) stresses in the transverse direction, and (*c*) stresses in the normal direction.

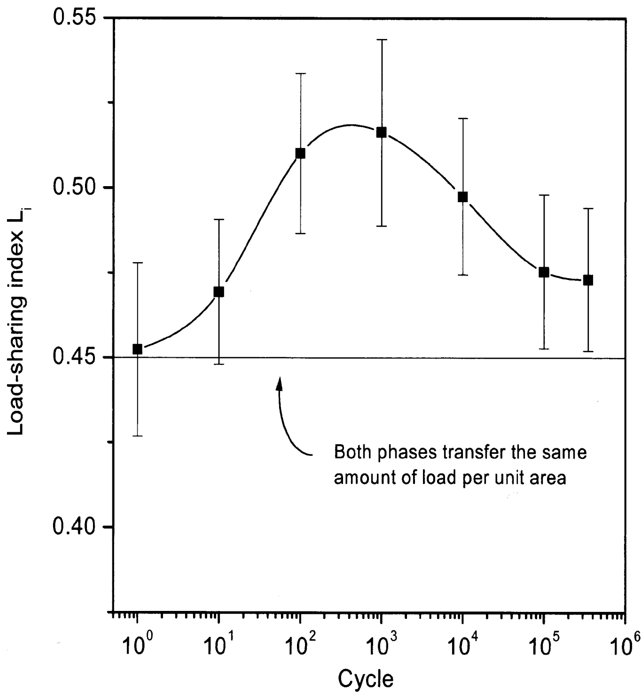

Fig. 6—Load-sharing index as a function of load cycle.

increase in the FWHM is observed for both phases, except for the maximum loading condition in the ferritic phase where a small decrease is observed.

C. *Texture Evolution*

For the as-received material, the ferritic phase showed two strong texture components, rotated cube texture $\{001\}\langle110\rangle$, and a component close to the Goss orientation $\{011\}\langle100\rangle$, both with a density of $\sim$6 times random. Several authors[22–25] have reported this type of texture for ferrite in duplex stainless steels. The austenitic phase shows weaker texture with the strongest component at the $\{011\}\langle111\rangle$ orientation with a density of $\sim$2.7 times random. The second strongest component is copper texture $\{112\}\langle111\rangle$ with a density of $\sim$2 times random. This type of texture is close to observations made by Ul-Haq *et al.*[24,25] for a similar material.

The evolution of the orientation density during fatigue for the different texture components is plotted in Figure 9. During fatigue, a clear trend toward stronger texture can be noticed in the ferritic phase. It is the rotated cube texture component $\{001\}\langle110\rangle$ that increases in intensity while the intensity close to the Goss orientation $\{011\}\langle100\rangle$ decreases. The changes in the austenitic phase are insignificant.

A crystallographic method based on the Voigt–Reuss–Hill assumption[26] was used to calculate the average elastic properties for the two phases in different directions. The input to this model are the measured ODF and the single-crystal elastic constants for each phase. The results for the as-received material are presented as polar plots in Figure 10. For the ferritic phase, the highest stiffness is found in the transverse direction (TD) and in the direction between the normal direction (ND) and the rolling direction (RD) (Figure 10(a)). Furthermore, a gradual increase of the stiffness isfound from RD toward TD. Due to the weak texture in the austenitic phase, only small variations in the elastic properties can be noticed for this phase (Figure 10(b)). Figure 10(c) shows the change in elastic properties in the ferritic phase due to cyclic loading. The stiffness decreases in all principal directions but increases for all directions close to 45 deg from ND. One can note that the change in the loading direction (RD) occurs during the very first cycles.

D. *Dislocation Structures*

Substructure evolution was investigated in detail by studying the dislocation structure in as-received material and in specimens fatigued with a maximum load of 500 MPa and a load ratio of $R = 0.05$ for l0^5 and $4.2 \cdot 10^5$ cycles. The latter corresponds to the fatigue life of the material at the investigated stress level.

The as-received material showed a low dislocation density in both phases (Figure 11(a)). Annealing twins were common in the austenitic phase due to the low stacking fault energy in this phase. However, after cyclic deformation, the dislocation density increased. After 10^5 load cycles, accumulation of dislocation arrays and small pileups of planar character were observed in the austenitic grains. Figure 11(b) shows that the planar arrays are formed by a set of extended dislocations lying on parallel slip planes. The stacking fault between two partials appears as a parallel fringe pattern. Meanwhile, in the interior ferritic grains, insignificant changes of the dislocation density were observed. This type of dislocation structure observed in the ferritic phase has previously been described by Mateo *et al.*[27] as a structure consisting of primary dislocations having predominantly screw character, either completely straight or with bowed segments, and small loops.

After $4.2\cdot10^5$ cycles, a denser dislocation structure was observed in both the ferritic and austenitic phases. In the austenitic phase, a dense distribution of planar arrays within the grains was also found. As shown in Figure 12(a), several subsets of straight dislocation segments consistent with the $\{111\}\langle110\rangle$ slip system are present, together with randomly oriented loops and half-loops. This type of array has been reported to form in the austenitic phase of duplex stainless steels during low-cycle fatigue at low-strain amplitudes.[27,28,29] One can also notice a denser dislocation structure close to phase boundaries and twin boundaries. In general, a lower dislocation density was found in the ferritic phase compared to the austenitic phase for the investigated foils. Some ferritic grains showed a substructure with massive pileups at the grain boundaries and a low dislocation density in the interior of the grain (Figure 12(b)), while others showed a homogeneous distribution of short dislocation segments.

The samples taken from the surface region showed a denser dislocation structure in the ferritic grains than the samples taken from the center of the fatigued specimen. Figure 11(c) shows a ferritic grain close to the surface that was fatigued for 10^5 cycles. One can notice formation of dislocation tangles and early formation of dislocation bundles. However, for the austenite, no significant difference in dislocation structure was noticed between the near-surface grains and the interior grains.

The surface of the specimens was also investigated by optical and electron microscopy. Slip bands were frequently

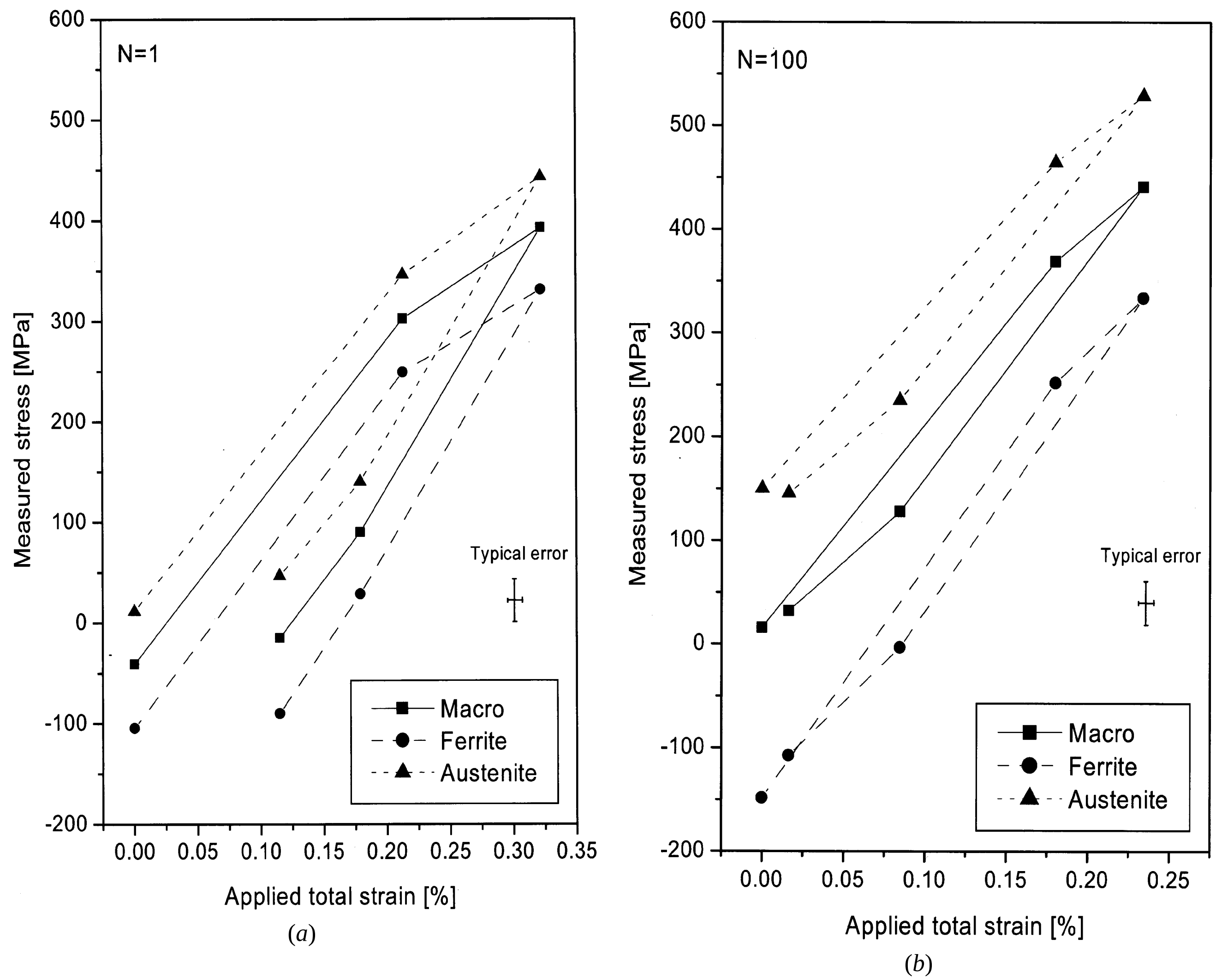

Fig. 7—Hysteresis loops for different fatigue cycles. (*a*) Load cycle $N = 1$, (*b*) load cycle $N = 100$, (*c*) load cycle $N = 10^3$, and (*d*) load cycle $N = 10^5$.

observed in the austenitic phase, while very few slip bands were seen in the ferritic phase.

IV. DISCUSSION

The *in situ* X-ray stress measurements are time consuming. For example, determination of the full stress tensor in both phases for a given applied load takes about 70 hours of X-ray beam time. During these measurements, some room temperature creep was observed, especially for the first load cycle, where a decrease in stress of 25 MPa was observed for an initial load of 500 MPa. In the following cycles, the decrease in applied stress during the measurement was lower, *e.g.*, a decrease of 6 MPa was observed during measurement at the maximum load after $3.5 \cdot 10^5$ cycles. This phenomenon, due to viscoelastic effects, cannot alone explain why the macroscopic stress range measured with X-rays is not consistent with the applied load measured by the load cell on the tensile device. However, the fact that a free surface is often less resistant to plastic deformation compared to the interior of the sample will lead to inhomogeneous plastic deformation through the thickness of the specimen.[30] Thus, less load is transferred through regions close to the surface compared to the interior. On the other hand, bcc metals have shown preferential cyclic hardening of the surface.[31] This effect, which is observed at small strain amplitudes, is due to the emergence and loss of mobile nonscrew dislocations at the free surface. The lack of mobile dislocations on the primary glide planes is compensated by activation of secondary glide systems, which results in a hardening of the surface.[31] It has further been suggested by Wang and Margolin[32] that the difference in flow stress between the surface and interior causes a Bauschinger effect for reversed loading. These abnormal surface phenomena are also apparent in the present study on duplex stainless steels because a more dense dislocation structure is observed in the ferritic surface grains compared to the interior ferritic grains (Figure 11(c)). The observed hardening of the surface also explains the increase of macrostress from −40 to 50 MPa in the loading direction for unloaded specimens (Figure 4(a)). Changes from compressive to tensile surface stresses have been reported for shot-peened two-phase brass and SAE 1040 steel during tension-tension fatigue.[33,34] Different dislocation microstructures in surface grains and interior grains have previously been found for ferritic grains in a duplex stainless steel of type 22.1Cr-5.4Ni-3.1Mo-0.11N after low cycle fatigue.[28] Nitrogen alloying provides a pronounced hardening in duplex stainless steels, and this strengthening

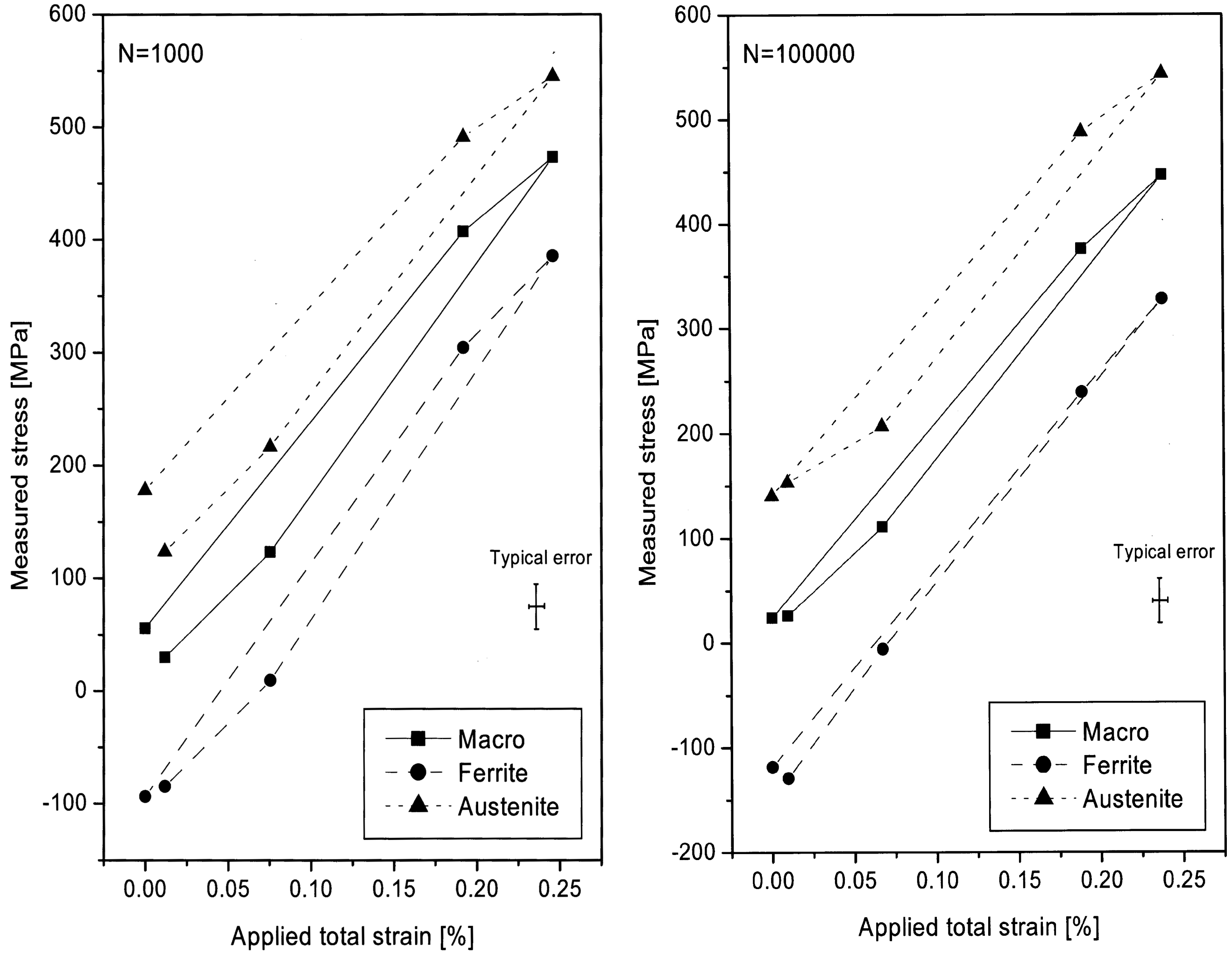

(*c*) (*d*)

Fig. 7—(Continued) Hysteresis loops for different fatigue cycles. (*a*) Load cycle $N = 1$, (*b*) load cycle $N = 100$, (*c*) load cycle $N = 10^3$, and (*d*) load cycle $N = 10^5$.

is mainly caused by hardening of the austenitic phase.[35] The material investigated in this study has a moderate nitrogen content (0.1 pct), and we have found in previous work[9] that both hardness and yield strength of this material were higher in the austenitic phase compared to the ferritic phase. It is also well known that tensile residual microstresses are present in the austenitic phase due to the higher coefficient of thermal expansion in this phase.[7,8,9]

During the first cycles, a rapid hardening is observed for the investigated stress level (Figure 3). Magnin and Lardon,[1] who noticed the same behavior for a duplex alloy of type 22.7Cr-7.0Ni-2.5Mo-0.07N during low-cycle fatigue, explained this behavior as a result of twinning in the ferritic phase. However, twinning was not observed as a significant mechanism in the cyclic response of the ferritic phase in this material. Mateo *et al.*[27] have suggested that twinning in the ferritic phase requires a minimum content of Ni and Mo, below which twinning is a suppressed deformation mode during cyclic loading. Both the Ni and Mo contents are lower in the investigated material compared to the material investigated by Magnin and Lardon. Hence, our observations confirm the predictions by Mateo *et al.*

Despite the lack of twinning in the ferritic phase, a rapid

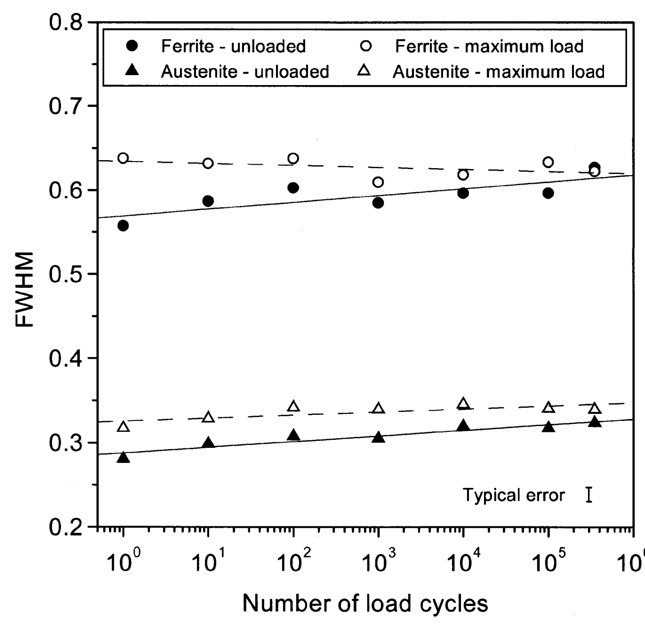

Fig. 8—Evolution of diffraction peak width as a function of load cycles for the ferrite {211} planes and the austenite {220} planes using Cr radiation.

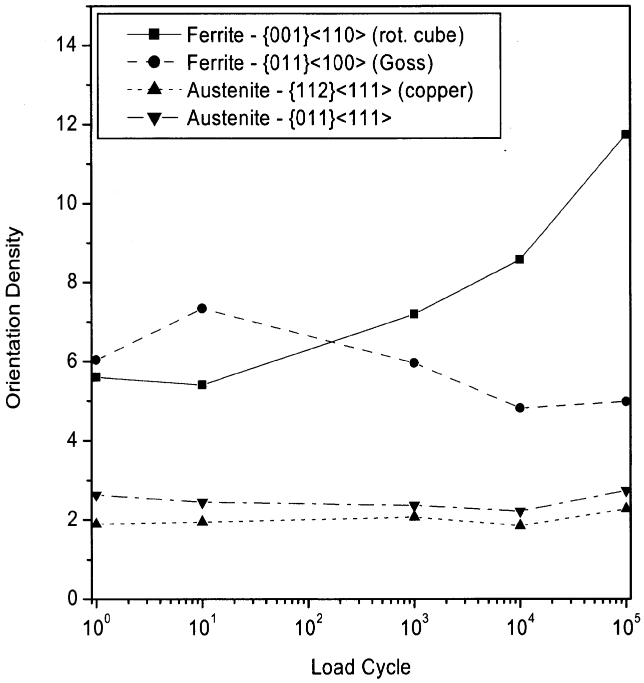

Fig. 9—Evolution of texture components during fatigue in a duplex stainless steel.

hardening is observed, and other deformation mechanisms must, therefore, account for the cyclic hardening effect. The hysteresis loops in Figure 7 indicate that plastic deformation always occurs to a higher degree in the austenitic phase compared to the ferritic phase. Pure austenitic stainless steels normally exhibit much higher work-hardening rates compared to pure ferritic materials, and it can, therefore, be assumed that the cyclic hardening is caused by work hardening in the austenitic phase. The high work-hardening rate in the austenitic phase has been associated to two different mechanisms.[35,36] First, the low stacking fault energy present in the austenitic phase is lowered even further by the presence of nitrogen. Second, the affinity between N and Cr induces short-range ordering. Both effects hinder cross-slip and promote planar slip, thereby increasing the strain-hardening rate. The pileups against grain and twin boundaries, observed in the transmission electron micrograph in Figure 11(b), indicate that a planar slip mode is active in the austenitic phase.

The X-ray stress measurements show that both phases deform plastically to almost the same degree during the first cycle, Figure 7(a), while higher microstresses are found in the austenitic phase after unloading due to the higher work hardening rate of the austenitic phase (Figure 4(a)). The compressive microstresses present in the ferritic phase prevent further plastic deformation in this phase, which explains why the widths of the hysteresis loops decrease in the ferritic phase but remain in the austenitic phase (Figure 7). These results are supported by the TEM investigations, where a denser dislocation structure was observed in the austenitic phase compared to the ferritic phase. After approximately 100 cycles, the microstresses reach a steady state for the unloaded specimen (Figure 4(a)). However, a slight increase of the microstress at the maximum load can be observed in the austenitic phase, and a clear drop in the load-sharing index also follows, as seen in Figure 6.

It is interesting to note that unloading does not appear to be purely elastic. This phenomenon was observed both on a macroscopic scale during mechanical testing, Figure 2, and during the *in situ* X-ray stress measurement, as in Figure 7. In both cases, the unloading curve bends close to 0 MPa during unloading for all tested load cycles. One source for such behavior is the back stress caused by the dislocation pileups. Because the net stress on a slip plane is the difference between the applied shear stress and back stress, unloading to zero stress after plastic straining could produce reversed plastic flow. This phenomenon, referred to as the Bauschinger effect, also explains why an increase in microstress is observed during unloading (Figure 7), because dislocation pileups were more frequently observed in the austenitic phase. If the dislocation pileups in the austenitic phase cause a Bauschinger effect, the unloading curve of this phase will not be linear but instead will decrease in slope close to the point where the material is completely unloaded. The Bauschinger effect, thus, produces a positive contribution to the tensile microstress in the austenitic phase during unloading. For equilibrium reasons, the compressive microstress in the ferrite also increases.

The load sharing between the two phases, shown in Figure 6, obviously depends on both elastic and plastic properties of both phases. Because the morphology of the two phases is elongated in the loading direction, the loading situation is expected to be closer to the isostrain condition than the isostress condition. Due to the higher elastic modulus of the ferritic phase, a higher load will, therefore, be transferred through ferrite in the elastic regime, and this is the reason why ferrite takes an overall larger load fraction. Nevertheless, for the first cycles, the effect due to the higher elastic modulus in the ferritic phase is compensated by that due to the higher yield strength of the austenitic phase, and both phases transfer almost the same amount of load per unit area. The increase of compressive residual microstresses in the ferritic phase due to inhomogeneous plastic deformation suppresses plastic deformation of the ferritic phase in the following cycles, and an increase in the load-sharing index is observed. The load sharing index reaches a maximum at $\sim$400 cycles followed by a slow decrease. The decrease in load sharing for the ferritic phase can also be seen in Figures 4 and 5, which show that the microstress for the austenitic phase increases at the maximum applied load while the microstress at the unloaded condition is almost unchanged. This implies a hardening of the austenitic phase at the surface without any further increase of residual micro and macrostresses.

The texture changes, observed during cyclic loading, were found to have minor influence on the elastic properties, Figure 10(c), and cannot account for the changes in load-sharing index. The texture changes are caused by crystal rotation or formation of new grains with a preferred orientation. Even if the cyclic response is determined mainly by the austenitic phase, the ferritic phase also deforms plastically. For a two-phase material, Bunge *et al.*[22] found that the phase with a smaller amount of local plasticity shows more pronounced textural changes than the phase with more local plasticity. The ferritic phase, with less plastic activity, is free to deform into the austenite with less interaction than in a single-phase material, but the deformation of the ferrite

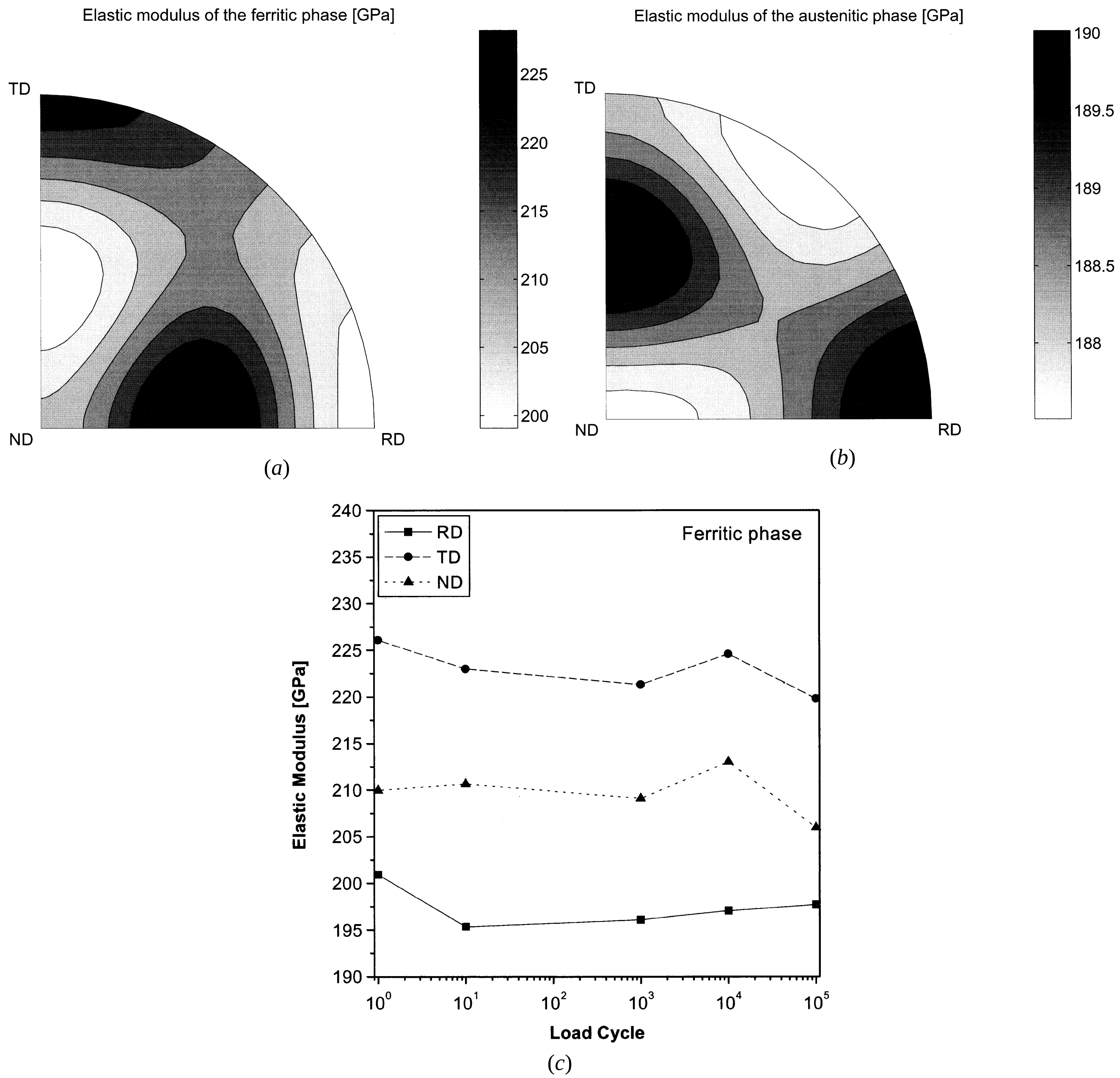

Fig. 10—Polar plots of the elastic modulus for (*a*) the ferritic phase and (*b*) the austenitic phase. (*c*) Evolution of the elastic modulus for the ferritic phase in different directions during fatigue.

must be compensated by some "turbulent" flow of the austenite,[22] which leads to an observed weakening of its texture.

In Figure 8, the FWHM for the diffracted peaks are plotted as a function of load cycle. An increase in the FWHM indicates that there is an increasing variation in lattice strain within one phase, which may have a number of different sources.[37] It is, however, interesting to see that the difference in peak width between the minimum and maximum loads during one cycle is bigger or comparable to the accumulated peak width increase between the first and last cycles in the unloaded condition. Thus, the elastic incompatibility contributes more than the plastic incompatibility to the variation in stress within one phase during cyclic loading. One can expect that this elastic incompatibility will lead to stress gradients and stress concentrations close to the phase boundaries, which is similar to what has been predicted by finite element simulations.[9] These stress concentrations contribute to microyielding close to phase boundaries, which suggests that the microyielding is sensitive to the morphology. An example of this can be found in Figure 12(a), which shows that the dislocation density in the austenitic matrix is higher close to the embedded ferritic island.

During fatigue, the differences in FWHM between the minimum and the maximum loads vanish for the ferritic phase (Figure 8). This indicates that the applied stress is taken up more uniformly in this phase, and the stress concentration sites in the ferrite are, thus, reduced during fatigue. The reduction of stress concentration sites in the ferritic phase requires rotation or formation of new grains, and this

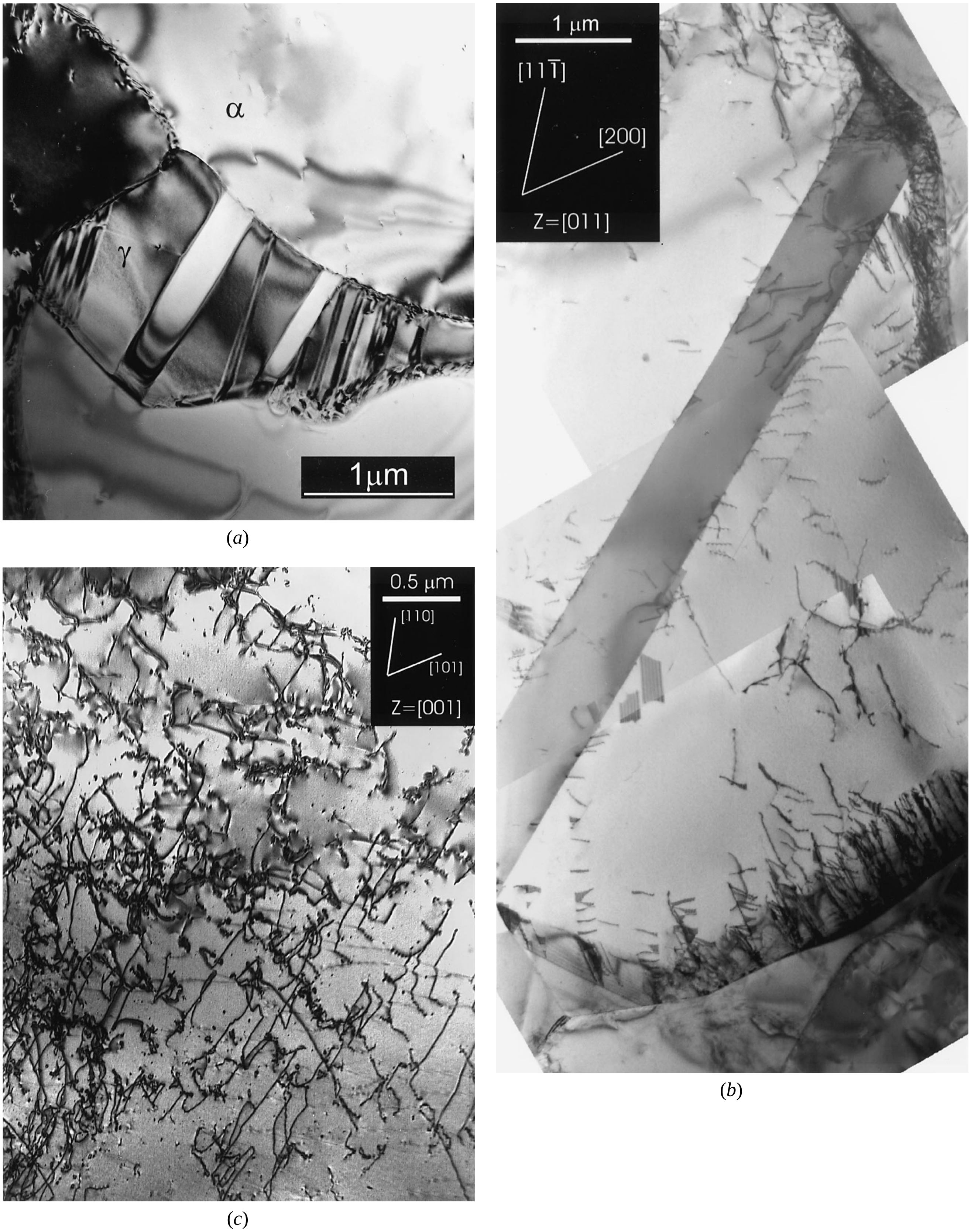

Fig. 11—Bright-field transmission electron micrographs. (*a*) The as-received material showing low dislocation density in both phases and twins in the austenite. (*b*) An austenitic grain fatigued for 10^5 cycles with a maximum stress of 500 MPa ($R = 0.05$). (*c*) A near-surface ferritic grain fatigued for 10^5 cycles.

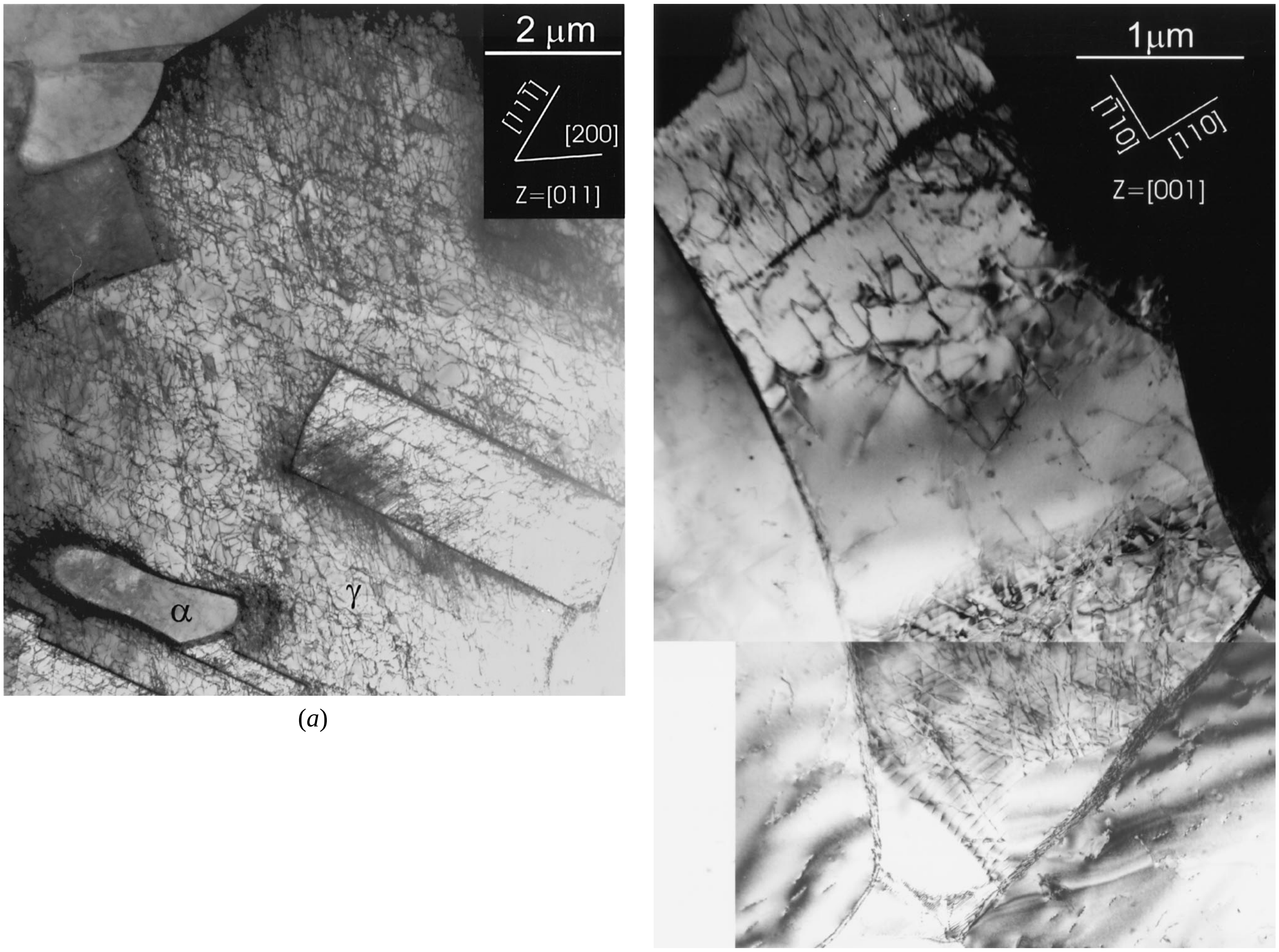

(*a*)

(*b*)

Fig. 12—(*a*) Bright-field transmission electron micrograph of austenitic grain fatigued for $4.2.10^5$ cycles. Note the high dislocation density in the vicinity of grain and twin boundaries. (*b*) Bright-field transmission electron micrograph of ferritic grain fatigued for $4.2 \cdot 10^5$ cycles.

correlates well with the observed texture changes in the ferritic phase (Figure 9).

In several studies where total strain controlled fatigue was performed, *e.g.*, References 13 and 14, fading of microstresses has been reported. We did not observe fading in this study when stress-controlled tension-tension fatigue ($R = 0.05$) was performed. In fact, an increase of the microstresses was observed, and the reason is the difference in plastic properties between the two phases and the accumulation of a mean plastic strain that takes place in every load cycle. It is obvious that the microstresses influence the cyclic response of the material and must be added to the applied stress when local strains are considered. Because the microstresses are compressive in the softer ferritic phase, the microstresses might act beneficial and delay crack initiation in the ferritic phase. However, if the microstresses are too large, crack initiation from local stress concentrations will instead occur in the austenitic phase.

V. SUMMARY

The behavior of a duplex stainless steel SAF 2304 during cyclic tension-tension loading with a maximum load of 500 MPa can be summarized as follows.

1. Rapid hardening was observed during the first cycle and was mainly attributed to work hardening of the austenitic phase due to planar dislocation movements causing pile-ups at twin and grain boundaries.
2. The rapid hardening of the austenitic phase contributed to increasing the residual microstresses in the austenitic phase from 50 to 140 MPa during the first 100 cycles. The cyclic loading response of the material was, thus, mainly controlled by the plastic properties of the austenitic phase.
3. Preferred hardening of the surface was observed, leading to a higher dislocation density in the surface grains compared to interior grains. As a result, an increase of surface residual macrostresses from -40 to 50 MPa was observed during the first 10^3 cycles. After the initial increase of microstress and macrostresses for the early cycles, no fading of residual stresses occurred for the following cycles.
4. Evolution of a more intense preferred orientation was observed in the ferritic phase during cyclic loading, while no significant change of the preferred orientation of the austenitic phase was found. The texture changes did not significantly change the elastic properties but contributed

to reduce the amount of stress concentration sites in the ferritic phase.

5. Even if the hardness and yield strength were found to be higher for the austenitic phase than the ferritic phase, X-ray stress analysis and TEM show that more plastic deformation occurs in the austenitic phase. A higher load, therefore, is transferred through the ferritic matrix because of the initial compressive residual stresses present in this phase.

ACKNOWLEDGMENTS

The work was financially supported by the Avesta Sheffield Research Foundation. Torsten Ericsson, Linköping University; Jan-Olof Nilsson, Sandvik Steel; and Hans Nordberg, Avesta Sheffield AB, are acknowledged for useful discussions.

REFERENCES

1. T. Magnin and J.M. Lardon: *Mater. Sci. Eng. A*, 1988, vol. A104, pp. 21-28.
2. T. Magnin, J. Lardon, and L. Coudreuse: *Low-Cycle Fatigue*, ASTM STP 942, ASTM, Philadelphia, PA, 1988, pp. 812-23.
3. F. Perdriset, T. Magnin, T. Cassange, P. Hoch, and F. Dupoiron: in *Duplex Stainless Steels '94*, T. Gooch, ed., TWI, Cambridge, United Kingdom, 1994, vol. 3.
4. J. Vogt, A. Messai, and J. Foct: in *Duplex Stainless Steels '94*, T. Gooch, ed., TWI, Cambridge, United Kingdom, 1994, vol. 1.
5. S. Degallaix, A. Seddouki, G. Degallaix, and J.-O. Nilsson: in *Fatigue '93*, J.-P. Bailon and J.I. Dickson, eds., Engineering Materials Advisory Services Ltd., Warley, United Kingdom, 1993, vol. 1, pp. 91-96.
6. J. Polak, S. Degallaix, and G. Degallaix: *Euromat 93: The 3rd Eur. Conf. on Advanced Materials and Processes*, R. Pichoir and P. Costa, eds., Les Éditions de Physique, Les Ulis Cedex A, France, 1993, vol. 1, pp. 679-84.
7. S. Harjo, Y. Tomota, and M. Ono: *Acta Mater.*, 1999, vol. 47, pp. 353-62.
8. K. Kamachi, T. Okada, M. Kawano, S. Namba, T. Ishida, N. Tani, and T. Kubohori: in *Progress in Science and Engineering of Composite, ICCM-IV*, T. Hayashi, K. Kawata, and S. Umekawa, eds., JSCM, Tokyo, 1982, pp. 1383-89.
9. J. Johansson, M. Odén, and X.-H. Zeng: *Acta Mater.*, 1999, vol. 47, pp. 2669-84.
10. T. Siegmund, F. Fischer, and E. Werner: *Mater. Sci. Eng.*, 1993, vol. A169, pp. 125-34.
11. I.C. Noyan and J.B. Cohen: *Residual Stress Measurement by Diffraction and Interpretation*, Springer-Verlag, New York, NY, 1987.
12. J.D. Almer, J.B. Cohen, and R.A. Winholtz: *Metall. Mater. Trans. A*, 1998, vol. 29A, pp. 2127-36.
13. J.D. Almer, J.B. Cohen, and B. Moran: *Mater. Sci. Eng.*, 2000, vol. 284, pp. 268-79.
14. R. Winholtz and J. Cohen: *Mater. Sci. Eng.*, 1992, vol. A154, pp. 155-63.
15. R. Winholtz and J. Cohen: *Metall. Trans. A*, 1992, vol. 23A, pp. 341-54.
16. I.C. Noyan: *Metall. Trans. A*, 1983, vol. 14A, pp. 1907-14.
17. R.A. Winholtz and J.B. Cohen: *Aust. J. Phys.*, 1988, vol. 41, pp. 189-99.
18. J.L. Lebrun and K. Inal: in *Advances in X-ray Analysis, Vol 40*, J.V. Gilfrich, T.C. Huang, C.R. Hubbard, I.C. Noyan, P.K. Predecki, D.K. Smith, and R.L. Snyder, International Centre for Diffraction Data, Newtown Square, PA, 1996, CD-rom.
19. K. Inal and J.L. Lebrun: in *ICRS-5*, T. Ericsson, M. Odén, and A. Andersson, eds., Linköping University, Linköping, 1997, vol. 1, pp. 472-77.
20. M. Barral, J. Lebrun, J. Sprauel, and G. Maeder: *Metall. Trans. A*, 1987, vol. 18A, pp. 1229-38.
21. H.J. Bunge: *Int. Mater. Rev.*, 1987, vol. 32, pp. 265-91.
22. H.J. Bunge, A. Ul-Haq, and H. Weiland: in *INFACON 6*, SAIMM, Johannesburg, 1992, vol. 2, pp. 197-201.
23. W. Hutchinson, K. Ushioda, and G. Runnsjö: *Mater. Sci. Technol.*, 1985, vol. 1, pp. 728-31.
24. A. Ul-Haq, H. Weiland, and H. Bunge: *J. Mater. Sci.*, 1994, vol. 29, pp. 2168-76.
25. A. Ul-Haq, H. Weiland, and H. Bunge: *Mater. Sci. Technol.*, 1994, vol. 10, pp. 289-98.
26. R. Hill: *Proc. Phys. Soc.*, 1952, vol. A65, pp. 349-54.
27. A. Mateo, L. Llanes, L. Itugoyen, and M. Anglada: *Acta Mater.*, 1996, vol. 44, pp. 1143-53.
28. T.P. Kruml, J. Polak, J. Obrtlik, and S. Degallaix: *Acta Mater.*, 1997, vol. 45, pp. 5145-51.
29. J. Polak, T. Kruml, and S. Degallaix: *Scripta Metall.*, 1993, vol. 29, pp. 1553-58.
30. E. Macherauch: *Exp. Mech.*, 1966, vol. 6, pp. 140-53.
31. H. Mughrabi: in *Dislocations and Properties of Real Materials*, M.H. Loretto, ed., The Institute of Metals, London, 1984, pp. 244-62.
32. Z. Wang and H. Margolin: *Acta Metall.*, 1986, vol. 34, pp. 721-33.
33. M. McClinton and J.B. Cohen: *Mater. Sci. Eng.*, 1982, vol. 56, pp. 259-63.
34. I.C. Noyan and J.B. Cohen: *Mater. Sci. Eng.*, 1985, vol. 75, pp. 179-93.
35. G. Wahlberg and G.L. Dunlop: *Proc. Stainless Steels '87*, Institute of Metals, London, 1987, pp. 291-99.
36. J.-O. Nilsson: *Scripta Metall.*, 1983, vol. 17, pp. 593-96.
37. B.E. Warren: *X-ray Diffraction*, Addison-Wesley, Reading, MA, 1969, pp. 251-313.